Magnetic Resonance in Medicine 63:1305–1314 (2010)

Dynamic Susceptibility Contrast MRI with Localized Arterial Input Functions

John J. Lee,[1] G. Larry Bretthorst,[2] Colin P. Derdeyn,[1,3,4] William J. Powers,[3,5] Tom O. Videen,[1,3] Abraham Z. Snyder,[1,3] Joanne Markham,[1] and Joshua S. Shimony[1]*

Compared to gold-standard measurements of cerebral perfusion with positron emission tomography using $H_2[^{15}O]$ tracers, measurements with dynamic susceptibility contrast MR are more accessible, less expensive, and less invasive. However, existing methods for analyzing and interpreting data from dynamic susceptibility contrast MR have characteristic disadvantages that include sensitivity to incorrectly modeled delay and dispersion in a single, global arterial input function. We describe a model of tissue microcirculation derived from tracer kinetics that estimates for each voxel a unique, localized arterial input function. Parameters of the model were estimated using Bayesian probability theory and Markov-chain Monte Carlo, circumventing difficulties arising from numerical deconvolution. Applying the new method to imaging studies from a cohort of 14 patients with chronic, atherosclerotic, occlusive disease showed strong correlations between perfusion measured by dynamic susceptibility contrast MR with localized arterial input function and perfusion measured by quantitative positron emission tomography with $H_2[^{15}O]$. Regression to positron emission tomography measurements enabled conversion of dynamic susceptibility contrast MR to a physiologic scale. Regression analysis for localized arterial input function gave estimates of a scaling factor for quantitation that described perfusion accurately in patients with substantial variability in hemodynamic impairment. Magn Reson Med 63:1305–1314, 2010. ©2010 Wiley-Liss, Inc.

Key words: cerebral perfusion; dynamic susceptibility contrast; positron emission tomography; magnetic resonance; carotid occlusion; hemodynamic impairment

Accurate measurement of cerebral hemodynamics advances our understanding of normal and abnormal brain physiology but remains a difficult research and clinical challenge (1). Many common disorders of the brain, including stroke and neoplasm, manifest through hemodynamic abnormalities and could be better diagnosed and treated with more accurate measurements (2,3).

The gold standard for quantitative, cerebral hemodynamic measurement is positron emission tomography (PET) using $H_2[^{15}O]$ for cerebral blood flow (CBF) and $C[^{15}O]$ for cerebral blood volume. However, PET is not as widely available as MR, and unlike MR, entails significant radiation exposure to the patient (4,5). Following the pioneering work by Østergaard et al. (6,7), cerebral hemodynamics measurements using dynamic susceptibility contrast (DSC) MR have become widely available on clinical scanners and have demonstrated early promise of clinical utility (2). Many variations of this method have been proposed (8–14), but few have been validated against a gold standard. Additionally, DSC MR methods yield relative measurements that require scaling to obtain quantitative physiologic values. This is typically done by assigning normal-appearing white matter a flow value of 20-22 mL/min/100 g of tissue (15).

Most clinical implementations of the DSC method require the selection of a large artery in the brain (usually a major branch of the middle cerebral artery) to define the arterial input function (AIF) used in the analysis of the data. Traditionally, the magnitude of the native MR signal is logarithmically transformed into relative units of gadolinium concentration. One difficulty with this transformation is that at the peak of the bolus passage, the signal may drop to the noise floor, making accurate estimates of concentration difficult (16,17).

The use of a single artery or several averaged artery measurements to represent the AIF for the whole brain has its origin in the earliest work in tracer kinetic methods (18,19). For quantitative PET, activity is measured directly from a peripheral arterial source. The resulting time-activity curve is then decay corrected and shifted in time to match the arrival of PET activity in the brain. One difference between the two methods relates to the use of a vascular tracer in DSC MR and a diffusible tracer in PET. Unlike DSC MR methods, which use the complete time-varying AIF, PET uses the convolution of the AIF with the response function (a decaying monoexponential). For these two reasons, flow measurements in DSC MR are significantly more sensitive than PET to errors in modeled delay and dispersion, as well as to the exact shape of the AIF (20). Several investigators have explored the use of local AIFs (LAIFs) to improve hemodynamic measurements (9,21,22), including the use

[1]Mallinckrodt Institute of Radiology, Washington University School of Medicine, St. Louis, Missouri, USA.

[2]Department of Chemistry, Washington University in St. Louis, St. Louis, Missouri, USA.

[3]Department of Neurology, Washington University School of Medicine, St. Louis, Missouri, USA.

[4]Department of Neurological Surgery, Washington University School of Medicine, St. Louis, Missouri, USA.

[5]Department of Neurology University of North Carolina School of Medicine, Chapel Hill, North Carolina, USA.

*Correspondence to: Joshua S. Shimony, MD, PhD, Mallinckrodt Institute of Radiology, Washington University School of Medicine, Campus Box 8131, St. Louis, MO 63110. E-mail: shimonyj@wustl.edu

Abbreviations: AIF: arterial input function; CBF: cerebral blood flow; CFS, cerebrospinal fluid; DSC: dynamic susceptibility contrast; EPI: echo-planar imaging; FLASH: fast low-angle shot; LAIF: localized arterial input function; MLEM: maximum-likelihood expectation-maximization; MTT: mean transit time; PET: positron emission tomography; ROI: region of interest; STLCOS: Saint Louis Carotid Occlusion Study; 3D: three-dimensional.

Received 2 July 2009; revised 4 November 2009; accepted 1 December 2009.

DOI 10.1002/mrm.22338
Published online in Wiley InterScience (www.interscience.wiley.com).

of voxel-specific AIFs using iterative blind deconvolution (23,24).

In this paper, we describe a variation of the standard tissue perfusion model (7) that provides a local estimate of both the AIF and the residue curve for each voxel in the brain. The parameters appearing in this model are estimated using Bayesian probability theory and Markov-chain Monte Carlo methods (25). This approach has several advantages over existing methods. Specifically, it eliminates the difficulty in selecting a single AIF by estimating one for each voxel in the brain. It does not require numerical evaluation of the logarithm of the signal, nor does it require numerical deconvolution. The new method estimates blood flow, blood volume, and mean transit time (MTT), as well as several additional model parameters, some of which may provide useful clinical information (25). Here we present the results of this method in comparison to PET measurements and to traditional DSC MR measurements performed on the same day in a population of patients with occlusive cerebrovascular disease (1,26).

THEORY

The magnetization observed by echo-planar imaging (EPI) from a bolus of contrast agent may be represented as (27):

$$S(t) = S_0 \exp[-k \cdot C_T(t)]. \quad [1]$$

The detected signal, $S(t)$, remains near a baseline value, S_0, until the arrival at time $t \equiv 0$ of the bolus, which is represented by the concentration time curve in the tissue, $C_T(t)$. k is an empiric constant of proportionality that varies with pulse sequence details, as well as details of the tissue microvasculature (6,7,27).

Conservation of mass and the fundamental central volume model of intravascular tracer kinetics (19) specify the concentration time curve in the tissue as a convolution of a voxel-dependent residue function, $R(t)$, with that voxel's AIF, $C_A(t)$:

$$C_T(t) = \mathrm{CBF} \cdot \int_0^t R(t-\tau) C_A(\tau) d\tau. \quad [2]$$

The residue function depends on the details of the tissue microstructure. CBF is the local CBF. A general expression for the residue function may be expressed as monoexponential, as conventionally used in PET, multiplied by a power series:

$$R(t) = e^{-t/\mathrm{MTT}} \left[1 + \sum_{n=1} c_n \left(\frac{t}{MTT} \right)^n \right] \quad [3]$$

Model selection methods were used to investigate the need for the additional parameters, c_n. For the quality of our data, the model probabilities consistently favored the simplest model, with $c_n = 0$ for all $n > 0$. Based on these calculations, we used a monoexponential residue function, similar to (7).

The bolus passage of the tracer was described as having three characteristic phases: (1) an initial rise in concentration with the main bolus arrival; (2) a subsequent rise in concentration from recirculation; and (3) a steady-state circulation phase. The concentrations of tracer in the main bolus, as well as in the recirculation peak, were each modeled with a normalized gamma function:

$$G(\alpha, \beta, t_0, t) = \frac{1}{\beta^{\alpha+1}\Gamma(\alpha+1)} (t - t_0)^{\alpha} \exp\left[-\frac{(t-t_0)}{\beta} \right] \quad [4]$$

The arrival time of the bolus is t_0, and the phenomenological parameter α quantifies the rapidity of arrival of contrast agent through the arterial network, while the parameter β quantifies the rapidity of washout via the venous network. A constant multiplied by a slowly rising exponential was used to model the gradual increase in the steady-state amount of contrast in the circulation, with γ representing this slow rise time. The model was not sensitive to the value of γ, which was set to 0.05. The complete model for the AIF at each voxel position was

$$C_A(t) \equiv c_0(1 - \exp(-\gamma(t - t_{01}))) + c_1 G(\alpha, \beta, t_{01}, t) + c_2 G(\alpha, \beta, t_{02}, t), \quad [5]$$

with $c_0 + c_1 + c_2 = 1$. In preliminary trials, the posterior probabilities of models used independent values for parameters $\{\alpha_1,\beta_1,t_{01}\}$ and $\{\alpha_2,\beta_2,t_{02}\}$ for the initial bolus and recirculation, respectively. Bayesian model selection showed the data were more consistent with a simpler model using a single set of dispersion parameters for both boluses $\{\alpha,\beta,t_{01},t_{02}\}$, but independent arrival times t_{01} and t_{02}. Equations 3-5 were substituted into Eq. 2 and integrals were evaluated analytically. The resulting closed-form expressions were substituted into Eq. 1. DSC MR provided time-dependent signals, $S(t)$, for each voxel. Parameter estimation was performed using Bayesian probability theory (25).

MATERIALS AND METHODS

Patient Selection

Subjects with paired hemodynamic PET and DSC MR studies were retrospectively identified by review of laboratory records. These subjects were studied under two different research protocols. All subjects provided written, informed consent in compliance with the institutional review board of the Washington University School of Medicine. Both protocols involved hemodynamic PET studies and DSC MR studies obtained on the same day for the purposes of correlative analysis. One protocol was a substudy of the Saint Louis Carotid Occlusion Study, a prospective, blinded, natural-history study of the role of hemodynamics in stroke risk for patients with atherosclerotic carotid artery occlusion (1,26). The other was a protocol specifically written for the purpose of comparing MR and PET methods of CBF measurement.

Fourteen subjects had complete PET and MR data suitable for analysis. Five and seven of these subjects have been previously reported in two correlative analyses of different MR methods (28,29). The primary inclusion

criterion for the 14 subjects was angiographically confirmed atherosclerotic occlusion of one proximal internal carotid artery. Both asymptomatic and symptomatic subjects were enrolled. Symptoms included transient ischemic neurologic deficits, transient monocular blindness, and mild to moderate permanent ischemic neurologic deficits in the appropriate carotid artery territory. Symptomatic subjects were studied at least 1 month after their last event. Exclusion criteria were inability to provide informed consent, inability to tolerate a supine position for PET and MRI, pregnancy, and contraindications to MRI, such as claustrophobia or MR-incompatible medical implants. PET and MR studies were obtained on the same day, without randomization, with the PET done first and the MRI following within approximately an hour of completion of the PET study.

PET Methods

All PET scans were performed on an ECAT EXACT HR PET scanner (CTI PET Systems, Knoxville, TN) run in two-dimensional mode with extended intersection septa. All subjects received antecubital intravenous lines for receiving fluids and radioactive tracers. A radial-artery catheter was placed and connected to an automated continuous blood sampler that recorded sampled activity in 1-sec bins. An attenuation scan was obtained. After venous injection of 50 to 75 mCi of $H_2[^{15}O]$ and following initial arrival of activity to the head, a 40-sec acquisition was recorded. PET scans were reconstructed with filtered back-projection, using ramp filtering. The nominal spatial resolution of the detector array was 2.14 × 2.14 × 3.125mm voxels. Back-projected PET activity counts were filtered with isotropic two-dimensional Gaussian kernels at 10.0mm full-width at half-maximum. CBF was measured using adaptations of the Kety autoradiographic method and permeability corrections (30,31).

CBF measurements with $H_2[^{15}O]$ and quantitative PET underestimate true CBF at high flows because of the incomplete permeability of the blood-brain barrier to water. Our measurements were corrected for this finite permeability using permeability-surface area products for water and butanol as described in Videen et al. (31). To the authors' best knowledge, these corrections have previously been reported in only one prior correlative study of perfusion measurements by PET and DSC MR (29).

MR Methods

All MR scans were performed on a 1.5-T Magnetom Vision scanner (Siemens, Erlangen, Germany). All subjects received a large-bore antecubital intravenous line appropriate for delivering normal saline and gadolinium contrast agent. Anatomic studies were performed with T_1-weighted three-dimensional (3D) fast low-angle shot (FLASH) gradient echo sequences with pulse repetition time/echo time = 18/8.4. Images were interpolated by the Vision console from 128 × 128 × 32 to 256 × 256 × 32 voxels; the field of view was 256 × 256 × 64mm. Immediately following an anatomic study, a dynamic study was performed with single-shot gradient EPI with pulse repetition time/echo time = 800/54 and 90° flip angles. Images were interpolated from 128 × 128 × 8 to 256 × 256 × 8 voxels; the field of view was 240 × 240 × 48mm. Axial EPI slices were contiguous and 6mm thick. The image sequence was repeated 80 times, for a total of 64 sec. Approximately 10 sec following the start of the EPI scan, a bolus of gadodiamide (Omniscan; Nycomed, Zurich, Switzerland) was intravenously administered by power injection (Mallinckrodt, Inc., St. Louis, MO) at 5 mL/sec, to a final dose of 0.2 mmol/kg.

LAIF Methods

Posterior probabilities for all model parameters were computed voxel by voxel, using complete EPI time series with Bayesian probability theory (32). There were 10 parameters per voxel, expressed in groups Ω_i with voxel indices i:

$$\Omega_i = \{CBF, MTT, t_{01}, t_{02}, \alpha, \beta, S_0, c_0, c_1, c_2\}_i \quad [6]$$

Two parameters were CBF and MTT. Two parameters expressed the primary and recirculation bolus arrival times, t_{01} and t_{02}. The shape of the arriving bolus was described by γ-variate parameters α and β. Finally, the remaining parameters described the baseline signal, S_0, and the relative size of the terms in the AIF (c_0, c_1, and c_2 in Eq. 5).

Bayes' theorem states that the posterior probability for the parameters, given data, D_i, and relevant background information, I, can be expressed as (32):

$$P(\Omega_i|D_i, I) \propto P(D_i|\Omega_i, I)P(\Omega_i|I), \quad [7]$$

for which $P(D_i|\Omega_i,I)$ is the likelihood of the data given the model parameters and $P(\Omega_i|I)$ is the prior probability for the model parameters. The prior probability was factored into independent prior probabilities for each parameter:

$$P(\Omega_i|I) \propto P(CBF|I)P(MTT|I)P(t_{01}|I)P(t_{02}|I)P(\alpha|I)P(\beta|I)\ldots \quad [8]$$

All prior probabilities were assigned Gaussian distributions bounded by appropriate physiologic ranges. The ranges selected for the parameters in our data set were *CBF* (0-20.0) (dimensionless units that include the empiric constant k); *MTT* (0-20.0) sec; t_{01} (0-40.0) sec; t_{02} (25.0-50.0) sec; α (0-12.0), β (0-6.0); c's (0-1.0). S_0 was set to a narrow range around the arbitrary baseline value produced by the MR scanner. The likelihood for the data from a voxel, given the model parameters $P(D_i|\Omega_i,I)$, is expressible as a marginal probability when the standard deviations, σ_i, are removed using the sum and product rules:

$$P(D_i|\Omega_i, I) = \int P(\sigma_i, D_i|\Omega_i, I)d\sigma_i \propto \int P(\sigma_i|I)P(D_i|\sigma_i, \Omega_i, I)d\sigma_i. \quad [9]$$

Assigning Jeffreys' prior probability to $P(\sigma_i|I)$ and assigning the Gaussian distribution to $P(D_i|\sigma_i,\Omega_i,I)$, the marginal probability for the data may be written as the

Student's t distribution:

$$P(D_i|\Omega_i, I) \propto \frac{1}{2}\Gamma\left(\frac{M}{2}\right)\left(\frac{Q_i}{2}\right)^{-M/2} \quad [10]$$

M is the number of data samples in time per voxel. Q_i is the total squared residual:

$$Q_i = \sum_{k=1}^{M}(E_{ik} - S_{ik})^2 \quad [11]$$

E_{ik} is the measured signal and S_{ik} is the model-estimated signal. The joint posterior probability was estimated using Markov-chain Monte Carlo, Metropolis-Hastings sampling, and simulated annealing.

Computational implementations were custom written for the SGI Origin 2000 (Silicon Graphics, Inc., Sunnyvale, CA). Using 32 processor cores, the computation time per image slice, with extraparenchymal voxels masked out, was approximately 1.8 h. Two of eight axial slices were analyzed for 14 of the subjects. Only one of eight axial slices was analyzed in one of the subjects. The framework is currently distributed as Varian VNMRJ packages (Varian, Inc., Palo Alto, CA) (http://bayesiananalysis.wustl.edu, http://www.varianinc.com/cgi-bin/nav?products/nmr/software/bayes). Recently, we have formulated a nonlinear algorithm that decreases the computation time by greater than 10-fold.

Deconvolution by Maximum-Likelihood Expectation Maximization

For comparison, perfusion was estimated using the method of maximum-likelihood expectation maximization (MLEM) originally reported by Vonken et al. (33). All computational details from the original implementation by Vonken et al. (33) were implemented, with two exceptions. First, all AIFs were expressed as absolute magnetizations in time and then smoothed, using nonlinear least-squares regression of γ-variate forms (Eq. 4). Second, the matrix representation of the AIF was forced to have the circulant-Toeplitz form advocated by Wu et al. (14). In a subset of the patient population described above, CBF maps from MLEM and oscillation-minimized singular-value decomposition had similar correlations with PET CBF maps. Limited tests of the sensitivity of our implementations of MLEM and oscillation-minimized singular-value decomposition revealed no observable dependence of AIFs on time shifts forward or backwards in time. On an IBM System x3655 (IBM, Armonk, NY) running one processor core, the computation time per image slice was approximately 0.8 h. AIFs were manually selected from perivascular voxels of M1-branches of the middle cerebral artery ipsilateral to patent carotid arteries. After identifying vessel-dominant voxels by scrolling through EPI time frames, eight to 10 voxels were selected in the vicinity of major vessel branches but exterior to areas of deep signal loss. Averaged AIFs were fitted with a γ-variate using nonlinear least squares (34).

PET MR Comparison

For each DSC-MR series, EPI time frames were coregistered to a single, early frame that best represented anatomic landmarks. 3D-FLASH series were aligned to the EPI spatial reference. $H_2[^{15}O]$ studies from PET were coregistered to the aligned 3D-FLASH. In some cases, coregistration was improved by using native 3D-FLASH as an intermediate spatial reference, e.g., PET was aligned to 3D-FLASH and then aligned PET was transformed to the EPI spatial reference. The final common processing for all series was transformation to the EPI reference. Linear, affine registration methods were used throughout. Minimization of mutual information was added in cases for which affine methods yielded inadequate alignment.

3D-FLASH images were segmented into three to five clusters using fuzzy c-mean clustering (Matlab 7; The MathWorks, Inc., Natick, MA). Each cluster was inspected and categorized as a region of interest (ROI) for gray matter, white matter, cerebrospinal fluid (CSF), extradural tissues, or bone. From EPI, voxels rich in arteries, those with the greatest signal drop during bolus passage, were identified and assigned to a separate, arterial ROI. All ROIs were graphically superimposed on coregistered 3D-FLASH, EPI, and PET series and visually inspected to ensure accuracy of placement. A board-certified neuroradiologist (J.S.S.) confirmed the accuracy of all placements.

Correlative analyses were performed using averages over contiguous blocks of in-plane, native voxels in CBF maps. CBF maps from PET and DSC MR were matched for partial-volume effects by using blocks of voxels sized to $10 \times 10 \times 6\text{mm}^3$. 3D Gaussian filtering was applied to native PET counts per validated methods prior to block averaging; filtering was never applied to MR CBF maps. High-resolution ROIs for arteries, CSF, and viable parenchyma were each block averaged and normalized for use with block-averaged CBF maps. Block-averaged ROIs were multiplied with block-averaged CBF maps. For block-averaged ROIs with mixed tissues, an approximate weighting scheme was used. The averaged ROI voxel was assigned a real value from zero through unity, the relative weight of the composite high-resolution tissue ROI voxels, each of which was always set to zero or unity by the clustered segmentation scheme. Each block average was analyzed with scatterplots and Bland-Altman plots.

All images were viewed and analyzed using Analyze AVW (Mayo Clinic, Rochester, MN), FSL (http://www.fmrib.ox.ac.uk/fsl) (35), diplib (Quantitative Imaging Group, Delft University of Technology, http://www.diplib.org), and Matlab (The Mathworks, Inc.).

RESULTS

Representative plots from the parameter estimation phase of the Bayesian processing in a single voxel are shown in Fig. 1. During the parameter estimation phase, the search space was explored using a Markov chain Monte-Carlo calculation and a population of parameter values was created by sampling this calculation and was used to compute mean and standard deviation estimates for each parameter. Figure 1a demonstrates the signal time curve of this voxel in red, with the model generated from the parameters that maximized the joint posterior probability in

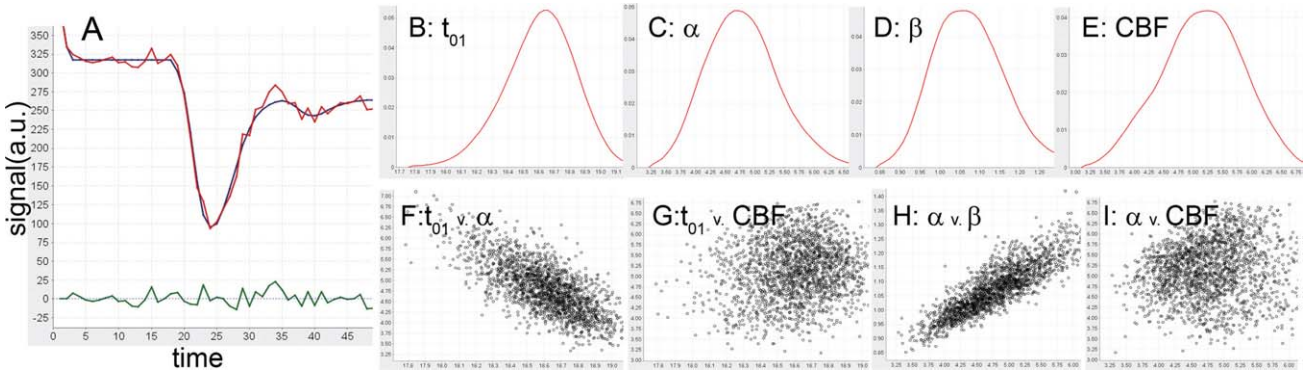

FIG. 1. Plots describe the parameter estimation phase of Bayesian processing for a single voxel. Parameter estimates were produced by sampling the Markov chain for the data model. **a:** The observed magnetization versus time in the selected voxel is plotted in red. Superposed in black is the model generated from parameters that maximized the joint posterior probability. The difference curve is plotted in green. Histograms of samples of the parameters **(b)** t_0, **(c)** α, **(d)** β, and **(e)** *CBF* display estimated probabilities along the vertical axes. Scatterplots of parameter pairs **(f)** t_0 versus α; **(g)** t_0 versus *CBF*; **(h)** α versus β; **(i)** α versus *CBF*; further details in the Results.

black and the difference in green. Figure 1b-e shows histograms of this sampling for four of the estimated parameters. The coefficients of variation (standard deviation divided by the mean) estimated from these plots is 1.4% for t_{01}, 12.3% for α, 8.1% for β, and 13.2% for the CBF. Figure 1f-i illustrates sampling for pairs of parameters, which provide information on cross-correlations between parameters in the model. The posterior probability density functions for t_{01} versus CBF and α versus CBF from Fig. 1g and i are consistent with no cross-correlation between the parameters. Although not shown, there was also no cross-correlation between CBF and β.

Details for a single patient from the study cohort are shown in Fig. 2. This 37-year-old female had a history of lacunar infarcts and infarction of the territory of the right middle-cerebral artery approximately 1 year prior to imaging. Cerebral angiography performed shortly before her MR and PET studies revealed the right internal carotid artery to be occluded. The T_1-weighted 3D-FLASH image shows the sequela of the patient's ischemic stroke, visible in the right hemisphere as encephalomalacia (radiologic display convention). The 3D-FLASH image was the reference for segmentation of ROIs and

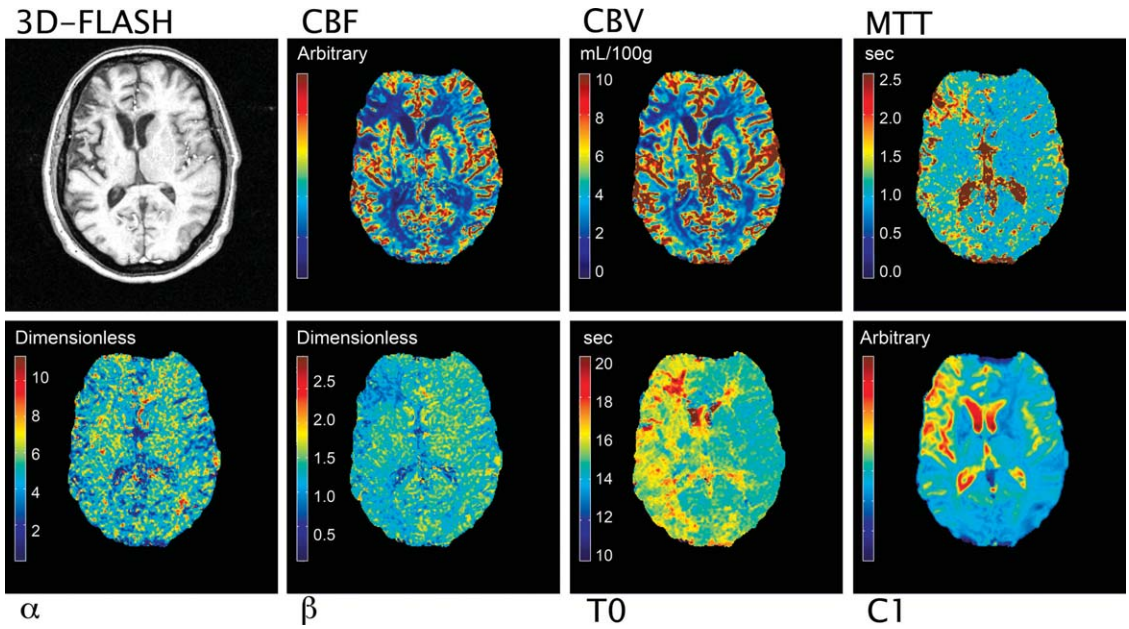

FIG. 2. T_1-weighted MR study and maps of hemodynamic parameters from the LAIF method for a patient with a history of lacunar infarcts and cerebral vascular accident involving the right middle-cerebral artery. CBF, cerebral blood volume, and MTT were estimated with LAIF. Additional tracer-kinetic parameters uniquely provided by LAIF are α, which characterizes the rapidity of inflow of contrast agent in the AIF; β, which characterizes the rate of outflow of contrast agent in the AIF; t_0, the time of arrival of the contrast agent tracer during its first passage through the cerebral circulation; and c_1, the relative weight of the concentration of the first passage of contrast agent to the time integral of concentration.

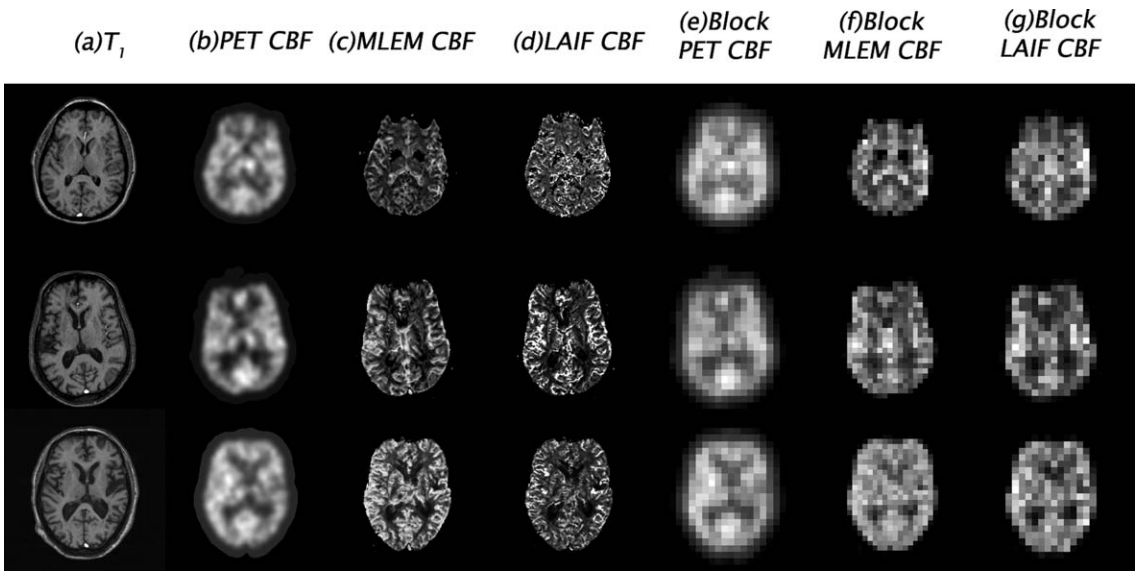

FIG. 3. CBF maps from MR LAIF and PET for three representative patients. Column **(a)** shows anatomic references. Columns **(b-d)** show CBF maps with native spatial resolutions for MR and PET. Columns **(e-g)** show results of block averaging to $10 \times 10 \times 6\text{mm}^2$, used to match differing spatial resolutions.

coregistration of PET images and is shown coregistered to EPI. Figure 2 shows maps of hemodynamic parameters obtained by MR LAIF: CBF, cerebral blood volume, MTT, α, β, t_{01}, and c_1. The right frontal area of infarction and hemispheric asymmetries are discernable in all parameter maps, except the map of α. This finding represents a uniform rate of inflow of contrast to both hemispheres, as may be expected from collateral blood supply to the hemisphere ipsilateral to chronic carotid occlusion. However, the map of β is asymmetric between hemispheres, likely representing slower venous outflow in the affected hemisphere. The map of t_0, the delay in bolus arrival, is dramatically asymmetric between hemispheres, showing delayed arrival in the hemisphere with complete carotid occlusion. The map of c_1 demonstrates increases in the affected hemisphere that correspond to decreases in the recirculation of contrast agent; the map corresponds anatomically with regions of decreased β. The affected hemisphere also exhibits mildly decreased CBF, mildly decreased cerebral blood volume, and increased MTT.

Representative blood-flow maps for three subjects from the study cohort are shown in Fig. 3. The variability of CBF maps between PET, MR LAIF, and MR MLEM, with and without block averaging of native voxels, is illustrated across columns. The variability of perfusion maps between human subjects is illustrated by the rows. Statistical analyses required comparison of perfusion maps from MR and PET with matched spatial resolutions. The results of block averaging are illustrated across the columns of Fig. 3. Not shown are the block-averaged ROIs used to exclude artery-rich voxels, CSF-rich voxels, voxels from extradural tissues, and background extracranial voxels.

Figure 4 illustrates graphically for a single patient the association of quantitative PET CBF to (Fig. 4a) MR LAIF CBF and (Fig. 4b) MR MLEM CBF. Each plotted point represents the average over a contiguous block of voxels; MR and PET voxels were each sized to $10 \times 10 \times 6$mm. Arbitrary units for LAIF and MLEM indicate that the value of scaling coefficient k is unknown. For the single, representative patient, the squared Pearson correlation coefficient of PET with LAIF is 0.493. For PET with MLEM, it is 0.446. The graphical analysis of Altman and Bland (36) for comparing alternative measurement methods is shown for (Fig. 4c) the deviation of standardized first moments of LAIF CBF from PET CBF and (Fig. 4d) the deviation of standardized first moments of MLEM CBF from PET CBF. Standardized moments show scale-invariant trends. Similar results were obtained for plots of percentage of the mean (37).

Figure 5 illustrates graphically for all 14 subjects the pooled association of PET CBF to (Fig. 5a) MR LAIF CBF and (Fig. 5b) MR MLEM CBF. Each plotted point represents a single block-averaged voxel. ROI masks were employed to exclude artery-rich voxels and CSF-rich voxels. The squared Pearson correlation coefficient for PET with LAIF is 0.314. For PET with MLEM, it is 0.246. The Bland and Altman analysis is shown for the pooled patient data for (Fig. 5c) the deviation of LAIF CBF from PET CBF and (Fig. 5d) the deviation of MLEM CBF from PET CBF. The scaling coefficient k is a priori not universal and constant for each patient, as illustrated previously by Takasawa et al. (37), as well as Fig. 5a and b. For any single patient, correlations are strong between LAIF and PET and between MLEM and PET, as detailed in Table 1. The mean value of k over 14 patients was calculated to be 0.054 ± 0.0089 for LAIF and 0.0068 ± 0.0013 for MLEM. Relative standard errors in k were 16% for LAIF and 19% for MLEM, suggesting that an empirically determined, constant k may be useful in practice.

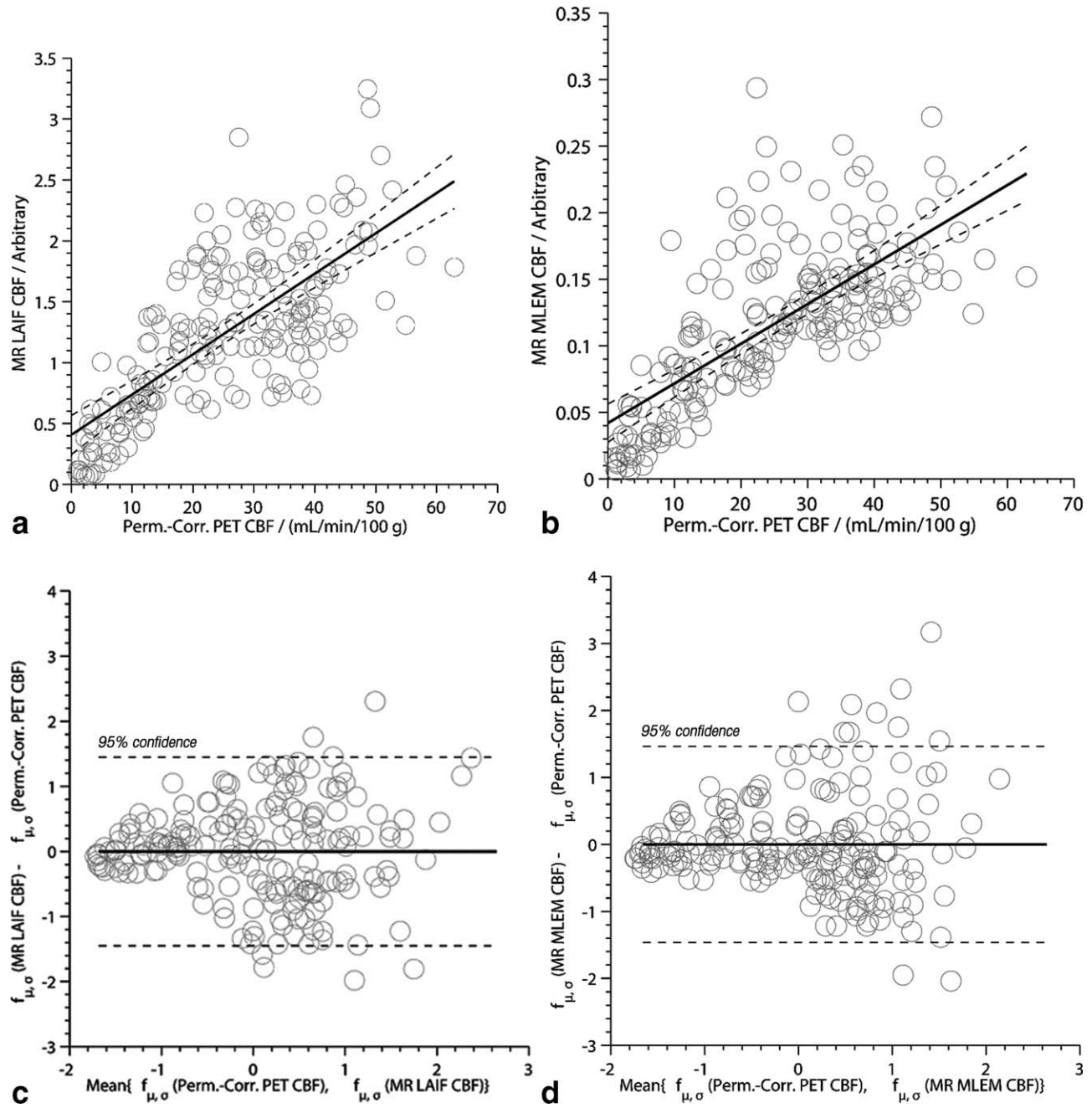

FIG. 4. Analysis of correlations between PET CBF and MR CBF for a representative patient (patient 1). Plotted points are block averages of parenchyma voxels only. Blocks containing a majority of CSF or artery-rich voxels are excluded. **a:** Scatterplot of PET CBF versus MR LAIF CBF. Linear regression yielded $CBF_{LAIF} = 0.407 + 0.0331\ CBF_{PET}$, which is plotted as a bold line. The 95% confidence interval for the fitted line with nonsimultaneous bounds are plotted with dashed lines. The squared Pearson product-moment correlation coefficient is 0.493. **b:** Similar plot of PET CBF versus MR MLEM CBF. Regression yielded $CBF_{MLEM} = 0.042 + 0.00298\ CBF_{PET}$. The squared correlation coefficient is 0.446. For Bland-Altman analysis of systematic trends, the standardized first moment of CBF values was used: $f_{\mu,\sigma}$. **c:** Differences between first moments of MR LAIF CBF and matching PET CBF are plotted with respect to the unbiased estimate of the true first moment of CBF, the average of first moments of MR LAIF CBF, and matching PET CBF. The 95% confidence intervals for differences are ±1.51. **d:** The difference between first moments of MR MLEM CBF and matching PET CBF is plotted against the unbiased estimate. The 95% confidence intervals for differences are ±1.60.

DISCUSSION

The LAIF method has several advantages over current techniques. The selection of a single, global AIF, which can be challenging in a DSC MR study, is obviated in LAIF. During contrast-bolus injection, the signal in large vessels will often saturate to the noise floor, making accurate estimation of the AIF difficult (16). It should be noted that this effect is unique to MR and is not shared by AIFs used in perfusion imaging by PET and CT.

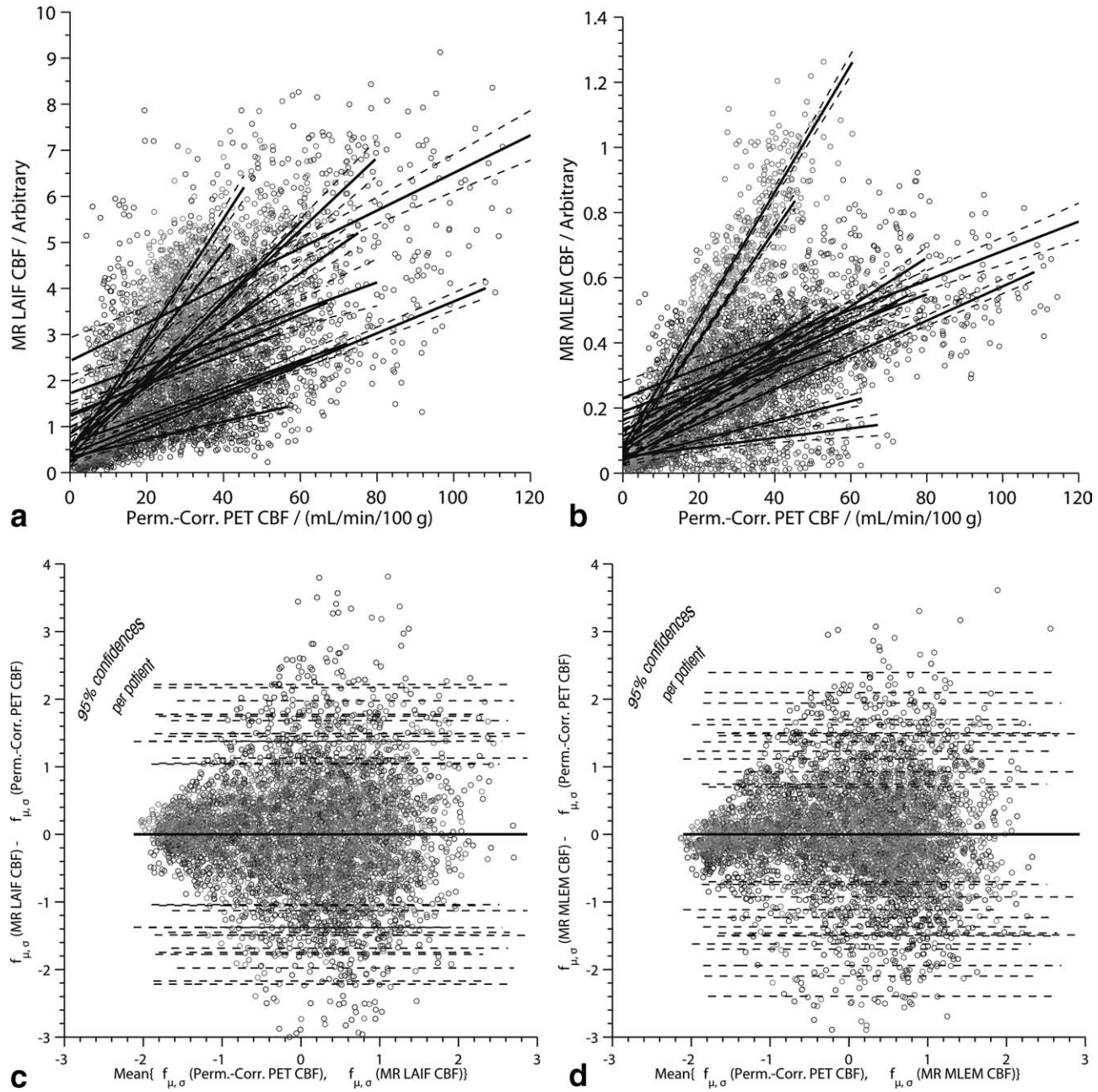

FIG. 5. The analysis of correlations described in Fig. 4 was applied to pooled PET and MR measurement from 14 patients. Plotted points are block averages of parenchyma voxels, with each patient assigned a unique gray value. **a:** Scatterplot of PET CBF versus MR LAIF CBF. For each patient, linear regression results are listed in Table 1; for each patient, regression and 95% confidence intervals are plotted with bold and dashed lines, respectively. Linear regression over pooled data from all 14 patients yielded $CBF_{LAIF} = 1.03 + 0.0483\ CBF_{PET}$, which is not plotted. The squared correlation coefficient is 0.314. **b:** Plot of PET CBF versus MR MLEM CBF. For each patient, linear regression results are listed in Table 1. Pooled regression yielded $CBF_{MLEM} = 0.155 + 0.00546\ CBF_{PET}$, which is not plotted. The squared correlation coefficient is 0.246. **c:** Bland-Altman analyses of the differences between the first moments of MR LAIF CBF and matched PET CBF versus the unbiased estimate of the true first moment of CBF, the average of first moments of MR LAIF CBF, and matching PET CBF. For each patient, 95% confidence intervals are plotted with dashed lines. Ninety-five percent confidence intervals for pooled mean differences from all 14 patients are ± 1.69, which is not shown. **d:** Bland-Altman analyses of the differences between the first moments of MR MLEM CBF and matched PET CBF versus the unbiased estimate of the true first moment of CBF. Ninety-five percent confidence intervals for pooled mean differences are ± 1.59.

Many investigators avoid voxels that are suspected to lie within or very near large vessels because of confounding effects from signal saturation. These criteria have been codified in automated AIF selection methods, which employ statistical clustering algorithms to segregate tissue concentration curves into groups with similar temporal shapes (38). A cluster is sought that best satisfies criteria such as large area under the curve of the concentration time curve, early arrival, rapidly and smoothly rising peak concentrations, and quick washout. Clusters are averaged, filtered, and often fitted with a γ-variate curve for use as the global AIF. Global AIF selection

Table 1
Scaling Factors, *k*, for MR LAIF and MR MLEM Methods*

Patient	k_{LAIF}	r^2_{LAIF}	k_{MLEM}	r^2_{MLEM}
1[a]	0.033	0.49	0.0028	0.446
2	0.079	0.53	0.0074	0.601
3	0.034	0.28	0.0039	0.315
4	0.106	0.53	0.0067	0.656
5	0.060	0.40	0.0072	0.385
6	0.034	0.65	0.0051	0.753
7	0.084	0.68	0.0192	0.843
8	0.036	0.22	0.0013	0.050
9	0.056	0.47	0.0059	0.539
10	0.129	0.69	0.0167	0.819
11	0.030	0.12	0.0032	0.116
12	0.029	0.66	0.0056	0.467
13	0.019	0.31	0.0067	0.388
14	0.029	0.11	0.0042	0.223

*The square of Pearson's correlation coefficients for regressions, r^2, are also shown.
[a]Data from patient 1 are shown in detail in Fig. 4.

methods run the risk of incorporating some tissue voxels into the AIF (39). The LAIF method models AIF saturation, using the assumption of a γ-variate shape, by directly using the MR signal (Eq. 1) without resorting to a logarithm transformation to concentrations.

Selection of a LAIF has the advantage of better representing the arterial supply to the brain in subjects with acute or chronic hemodynamic impairment. Using a single AIF provides accurate results in perfusion imaging with quantitative PET since PET uses the convolution integral of the AIF rather than its time course. Additionally, PET uses a diffusible tracer for which the residue curve is an exponential that requires the estimation of a single transit-time parameter. Compared to the use of AIFs in PET, the use of AIFs for DSC MR is significantly more sensitive to the effects of delay and dispersion. Underestimations, as well as overestimations, of regional CBF have been observed and attributed to the delay, dispersion, and mixing with tissue voxels that result from the construction of a global AIF (14,39,40). Delay and dispersion in the AIF are hallmarks of hemodynamic impairment; thus, DSC MR with deconvolution may compound inaccuracies in this clinical scenario. The significant variations from normal cerebral hemodynamics in our patient cohort bring out these overestimations and underestimations in Fig. 5. Delay, but not dispersion, effects may be substantially mitigated by ensuring that numerical deconvolutions are performed with circulant-Toeplitz kernels, thereby preserving temporal causality (14). There is great variability in perfusion measurements with variations in the choice of AIFs, as has been shown in numerous studies (39,41,42). The LAIF method avoids the complications of delay and dispersion from a distal AIF.

An additional benefit of the LAIF model is the estimation of new parameters that may provide additional valuable clinical information. These parameters include the arrival time for the main bolus and the recirculation peak (t_{01} and t_{02}) and the LAIF γ-variate parameters α and β. The difference between t_{01} and t_{02} is an estimate of the circulation time of the bolus and may provide some information on the cardiac output of the subject. Since α determines the rapidity of the rise of the AIF, it may provide information on the arterial supply to the voxel. A slow rise time may indicate local cerebrovascular disease or collateral supply. The β parameter determines the descending portion of the AIF and thus may provide information on the capillary and venous drainage from the voxel in question. Delayed drainage of contrast could indicate venous congestion due to venous thrombosis or a nearby arterial-venous anomaly.

Within the limitation of our assumption of certain shapes for the AIF and residue curves, the LAIF method avoids the need to perform numerical deconvolution, which is inherently unstable, especially with non-Gaussian noise. Various methods have been developed to overcome this problem: truncating the rank of the deconvolution kernel by singular-value decomposition (14), Tikhonov regularization (8), and also regularization by parameterized reduction of oscillations in the residue function (40,43). The LAIF model makes the assumption of analytical curve shapes for the tissue concentration curve and the residue curve and then, using these analytical curves, performs an analytical convolution. The parameter estimation then relies on Bayesian probability theory and Markov-chain Monte Carlo and does not require computation of deconvolutions, thus avoiding these issues altogether.

It should be noted that when substituting Eq. 2 into Eq. 1, the CBF is multiplied by the unknown constant *k*, and without a way to determine *k* only relative perfusion can be evaluated. In this study, we show that PET perfusion data may be used to calibrate this constant for a population of patients with chronic, cerebral hemodynamic impairment. Although theoretically *k* varies across different tissue types and details of pulse sequences, in practice, a single value may be adequate for the MR CBF ranges of clinical significance. The determination of this constant may provide a scaling factor to better quantify flow measurements with DSC MR.

CONCLUSION

We present a tissue perfusion model that provides a local estimate of both the AIF and the residue function for each voxel in brain perfusion image. The parameters of the model are estimated using Bayesian probability theory and Markov-chain Monte Carlo. This technique has several advantages over existing methods. It obviates the difficulties of determining a single, global AIF. It does not require numerical deconvolution. In addition to estimating CBF, cerebral blood volume, and MTT, several novel model parameters are estimated, which may provide useful clinical information.

ACKNOWLEDGMENTS

We thank the ASNR Neuroradiology Education and Research Foundation, Boston Scientific-Target Fellowship in Cerebrovascular Disease Research (J.S.S.), and the Mallinckrodt Institute of Radiology–Bayer Healthcare Clinical Research Fellowship (J.J.L.) for their generous support during this project. PET and MR data acquisition was supported by National Institutes of Health research grants R01 28497 (W.J.P.) and K08 NS02029 (C.P.D.)

REFERENCES

1. Grubb RL Jr, Derdeyn CP, Fritsch SM, Carpenter DA, Yundt KD, Videen TO, Spitznagel EL, Powers WJ. Importance of hemodynamic factors in the prognosis of symptomatic carotid occlusion. JAMA 1998;280:1055–1060.
2. Gonzalez RG. Acute ischemic stroke: imaging and intervention. Berlin, Germany: Springer-Verlag; 2005. 268 p.
3. Zazulia AR, Markham J, Powers WJ. Cerebral blood flow and metabolism in human cerebrovascular disease. In: Mohr JP, editor. Stroke: pathophysiology, diagnosis, and management. Philadelphia, PA: Churchill and Livingstone; 2004. 1591 p.
4. Powers WJ, Raichle ME, Grubb RL Jr. Positron emission tomography to assess cerebral perfusion. Lancet 1985;1:102–103.
5. Powers WJ, Zazulia AR. The use of positron emission tomography in cerebrovascular disease. Neuroimag Clin N Am 2003;13:741–758.
6. Østergaard L, Sorensen AG, Kwong KK, Weisskoff RM, Gyldensted C, Rosen BR. High resolution measurement of cerebral blood flow using intravascular tracer bolus passages, part II: experimental comparison and preliminary results. Magn Reson Med 1996;36:726–736.
7. Østergaard L, Weisskoff RM, Chesler DA, Gyldensted C, Rosen BR. High resolution measurement of cerebral blood flow using intravascular tracer bolus passages, part I: mathematical approach and statistical analysis. Magn Reson Med 1996;36:715–725.
8. Calamante F, Gadian DG, Connelly A. Quantification of bolus-tracking MRI: improved characterization of the tissue residue function using Tikhonov regularization. Magn Reson Med 2003;50:1237–1247.
9. Calamante F, Morup M, Hansen LK. Defining a local arterial input function for perfusion MRI using independent component analysis. Magn Reson Med 2004;52:789–797.
10. Grandin CB, Bol A, Smith AM, Michel C, Cosnard G. Absolute CBF and CBV measurements by MRI bolus tracking before and after acetazolamide challenge: repeatability and comparison with PET in humans. Neuroimage 2005;26:525–535.
11. Grandin CB, Duprez TP, Smith AM, Oppenheim C, Peeters A, Robert AR, Cosnard G. Which MR-derived perfusion parameters are the best predictors of infarct growth in hyperacute stroke? Comparative study between relative and quantitative measurements. Radiology 2002; 223:361–370.
12. Perkio J, Aronen HJ, Kangasmaki A, Liu Y, Karonen J, Savolainen S, Østergaard L. Evaluation of four postprocessing methods for determination of cerebral blood volume and mean transit time by dynamic susceptibility contrast imaging. Magn Reson Med 2002;47:973–981.
13. Sourbron S, Luypaert R, Van Schuerbeek P, Dujardin M, Stadnik T. Choice of the regularization parameter for perfusion quantification with MRI. Phys Med Biol 2004;49:3307–3324.
14. Wu O, Østergaard L, Weisskoff RM, Benner T, Rosen BR, Sorensen AG. Tracer arrival timing-insensitive technique for estimating flow in MR perfusion-weighted imaging using singular value decomposition with a block-circulant deconvolution matrix. Magn Reson Med 2003; 50:164–174.
15. Østergaard L, Smith DF, Vestergaard-Poulsen P, Hansen SB, Gee AD, Gjedde A, Gyldensted C. Absolute cerebral blood flow and blood volume measured by magnetic resonance imaging bolus tracking: comparison with positron emission tomography values. J Cereb Blood Flow Metab 1998;18:425–432.
16. Calamante F, Vonken EJ, van Osch MJ. Contrast agent concentration measurements affecting quantification of bolus-tracking perfusion MRI. Magn Reson Med 2007;58:544–553.
17. Duhamel G, Schlaug G, Alsop DC. Measurement of arterial input functions for dynamic susceptibility contrast magnetic resonance imaging using echoplanar images: comparison of physical simulations with in vivo results. Magn Reson Med 2006;55:514–523.
18. Lassen NA, Perl WP. Tracer kinetic models in medical physiology. New York: Raven Press; 1979. 189 p.
19. Meier P, Zierler KL. On the theory of the indicator dilution method for measurement of blood flow and volume. J Appl Physiol 1954;6: 731–744.
20. Calamante F, Willats L, Gadian DG, Connelly A. Bolus delay and dispersion in perfusion MRI: implications for tissue predictor models in stroke. Magn Reson Med 2006;55:1180–1185.
21. Alsop D, Wedmid A, Schlaug G. Defining a local input function for perfusion quantification with bolus contrast MRI. In: The 10th Annual Meeting of the International Society for Magnetic Resonance in Medicine. Honolulu, HI, 2002. p 659.
22. Ducreux D, Buvat I, Meder JF, Mikulis D, Crawley A, Fredy D, Ter-Brugge K, Lasjaunias P, Bittoun J. Perfusion-weighted MR imaging studies in brain hypervascular diseases: comparison of arterial input function extractions for perfusion measurement. AJNR Am J Neuroradiol 2006;27:1059–1069.
23. Gruner R, Bjornara BT, Moen G, Taxt T. Magnetic resonance brain perfusion imaging with voxel-specific arterial input functions. J Magn Reson Imaging 2006;23:273–284.
24. Gruner R, Taxt T. Iterative blind deconvolution in magnetic resonance brain perfusion imaging. Magn Reson Med 2006;55:805–815.
25. Shimony JS, Lee JJ, Bretthorst GL. Estimation of cerebral blood flow from dynamic susceptibility contrast MRI using a tissue model. Bayesian inference and maximum entropy methods in science and engineering. Am Inst Physics 2005;803:535–542.
26. Powers WJ, Press GA, Grubb RL, Gado M, Raichle ME. The effect of hemodynamically significant carotid artery disease on the hemodynamic status of the cerebral circulation. Ann Intern Med 1987;106: 27–35.
27. Villringer A, Rosen BR, Belliveau JW, Ackerman JL, Lauffer RB, Buxton RB, Chao YS, Wedeen VJ, Brady TJ. Dynamic imaging with lanthanide chelates in normal brain: contrast due to magnetic susceptibility effects. Magn Reson Med 1988;6:164–174.
28. Lin W, Celik A, Derdeyn C, An H, Lee Y, Videen T, Østergaard L, Powers WJ. Quantitative measurements of cerebral blood flow in patients with unilateral carotid artery occlusion: a PET and MR study. J Magn Reson Imaging 2001;14:659–667.
29. Mukherjee P, Kang HC, Videen TO, McKinstry RC, Powers WJ, Derdeyn CP. Measurement of cerebral blood flow in chronic carotid occlusive disease: comparison of dynamic susceptibility contrast perfusion MR imaging with positron emission tomography. AJNR Am J Neuroradiol 2003;24:862–871.
30. Herscovitch P, Markham J, Raichle ME. Brain blood flow measured with intravenous $H_2(15)O$, I: theory and error analysis. J Nucl Med 1983;24:782–789.
31. Videen TO, Perlmutter JS, Herscovitch P, Raichle ME. Brain blood volume, flow, and oxygen utilization measured with ^{15}O radiotracers and positron emission tomography: revised metabolic computations. J Cereb Blood Flow Metab 1987;7:513–516.
32. Jaynes ET, Bretthorst GL. Probability theory: the logic of science. New York: Cambridge University Press; 2003. 727 p.
33. Vonken EP, Beekman FJ, Bakker CJ, Viergever MA. Maximum likelihood estimation of cerebral blood flow in dynamic susceptibility contrast MRI. Magn Reson Med 1999;41:343–350.
34. Bretthorst GL. Bayesian spectrum analysis and parameter estimation. New York: Springer-Verlag; 1988. 209 p.
35. Smith SM, Jenkinson M, Woolrich MW, Beckmann CF, Behrens TE, Johansen-Berg H, Bannister PR, De Luca M, Drobnjak I, Flitney DE, Niazy RK, Saunders J, Vickers J, Zhang Y, De Stefano N, Brady JM, Matthews PM. Advances in functional and structural MR image analysis and implementation as FSL. Neuroimage 2004;23(suppl 1): S208–219.
36. Altman DG, Bland JM. Measurement in medicine: the analysis of method comparison studies. Statistician 1983;32:307–317.
37. Takasawa M, Jones PS, Guadagno JV, Christensen S, Fryer TD, Harding S, Gillard JH, Williams GB, Aigbirhio FI, Warburton EA, Østergaard L, Baron JC. How reliable is perfusion MR in acute stroke? Validation and determination of the penumbra threshold against quantitative PET. Stroke 2008;39:870–877.
38. Mouridsen K, Christensen S, Gyldensted L, Østergaard L. Automatic selection of arterial input function using cluster analysis. Magn Reson Med 2006;55:524–531.
39. Wu O, Østergaard L, Sorensen AG. Technical aspects of perfusion-weighted imaging. Neuroimaging Clin N Am 2005;15:623–637, xi.
40. Wu O, Østergaard L, Koroshetz WJ, Schwamm LH, O'Donnell J, Schaefer PW, Rosen BR, Weisskoff RM, Sorensen AG. Effects of tracer arrival time on flow estimates in MR perfusion-weighted imaging. Magn Reson Med 2003;50:856–864.
41. Calamante F, Gadian DG, Connelly A. Quantification of perfusion using bolus tracking MRI in stroke: assumptions, limitations, and potential implications for clinical use. Stroke 2002;33:1146–1151.
42. van Osch MJ, van der Grond J, Bakker CJ. Partial volume effects on arterial input functions: shape and amplitude distortions and their correction. J Magn Reson Imaging 2005;22:704–709.
43. Gobbel GT, Fike JR. A deconvolution method for evaluating indicator-dilution curves. Phys Med Biol 1994;39:1833–1854.